

*dHybridR*: a Hybrid–Particle-in-Cell Code Including Relativistic Ion Dynamics

COLBY C. HAGGERTY<sup>1</sup> AND DAMIANO CAPRIOLI<sup>1</sup>

<sup>1</sup>*Department of Astronomy and Astrophysics, University of Chicago, 5640 S Ellis Ave, Chicago, IL 60637, USA*

(Received January 1, 2018; Revised January 7, 2018; Accepted May 6, 2022)

ABSTRACT

We present the first plasma simulations obtained with the code `dHybridR`, a hybrid particle-in-cell code with fluid electrons and kinetic relativistic ions. `dHybridR` is perfectly suited for all the astrophysical and space-physics problems where a few energetic non-thermal particles (i.e., Cosmic Rays, CRs) affect the overall dynamics of a non-relativistic plasma, such as CR-driven instabilities, collisionless shocks, magnetic reconnection, turbulence, etc. In this method paper we provide some applications to linear (resonant/non-resonant CR streaming instability) and strongly non-linear (parallel shocks) problems that show the capabilities of the code. In particular, we provide the first self-consistent hybrid runs that show the acceleration of relativistic ions at non-relativistic shocks; CRs develop a power-law in momentum, which translates to a broken power law in energy that exhibits a steepening around the ion rest mass, as predicted by the theory of diffusive shock acceleration. To outline the vast range of possible applications of `dHybridR`, we show some examples of 2D runs relevant for fast shocks in radio supernovae, whose evolution can be followed in real time, and 3D runs of low-Mach-number heliospheric shocks, which can be compared with in-situ spacecraft observations.

1. INTRODUCTION

Understanding the generation and dynamical effects of non-thermal, high-energy particles (Cosmic Rays, CRs) in astrophysical plasmas has been an important question since their discovery in the early 20<sup>th</sup> century. CRs are ubiquitous throughout the universe and in the Galactic interstellar medium are in equipartition with the thermal plasma and the magnetic fields, despite being very few in number, about  $10^{-9}$  times less abundant than thermal protons.

Self-consistent modeling of the non-linear interplay between CRs, thermal plasma, and magnetic fields is a challenging problem and requires kinetic numerical approaches; moreover, such a non-linear physics inherently spans multiple length and time scales. While CR acceleration typically occurs on length/time scales comparable with space/astro-physical scales (the gyroradius of a GeV particle is about  $10^{12}$ cm in a  $\mu$ G magnetic field), thermal particles and electro-magnetic fields evolve on much smaller plasma scales (electron/ion skin depths are typically of the order of a few to hundreds km).

Fully kinetic plasma models (like Particle-In-Cell, PIC, or Vlasov codes) can accurately model all of the relevant physics for these systems (e.g., Birdsall & Langdon 1991; Bell et al. 2006; Valentini et al. 2007; Lapenta 2012; Palmroth et al. 2018), however resolving electron dynamics requires such small grid sizes and time steps that simulating systems with CRs becomes numerically prohibitively expensive.

The hybrid model, which treats ions as kinetic macroparticles that satisfy the Vlasov and Lorentz force equations and electrons as a fluid that keeps the system charge neutral, can self-consistently bridge thermal and non-thermal regimes; hybrid models (see Winske & Omid 1996; Lipatov 2002, for reviews) have been used to study many different plasma problems including shocks, turbulence and magnetic reconnection (e.g., Byers et al. 1978; Hewett & Nielson 1978; Gargaté et al. 2010; Burgess et al. 2016; Giacalone et al. 1992; Caprioli & Spitkovsky 2014a; Karimabadi et al. 2014; Le et al. 2009; Kunz et al. 2014).

A significant limitation to the hybrid model, however, is that the speed of light is typically taken to be infinitely large, forcing all of the ion dynamics to be classical. This restriction is significant for modeling the physics of CRs and may raise concern when simulations are compared with observations.

Alternative approaches have used a kinetic description of CRs, while treating the thermal population as a magneto-hydrodynamical (MHD) fluid (e.g., Zachary & Cohen 1986; Lucek & Bell 2000; Bai et al. 2015; van Marle et al. 2018; Mignone et al. 2018; Dubois et al. 2019). While these MHD-PIC simulations can capture some CR physics, the gap between thermal and energetic particles requires the injection of CRs in the system to be externally prescribed, rather than modeled from first principles.

In this work we present the first –to our knowledge– hybrid code that includes relativistic ion dynamics, `dHybridR`, which is built upon the massively-parallel Newtonian code `dHybrid` (Gargaté et al. 2007). In Section 2 we outline the basics of the code and we argue that the set of systems with both thermal and CR populations can be modeled this way without violating any of the hybrid approximations. In Section 3 we compare `dHybridR` simulations of CR streaming instabilities with linear theory predictions and show that the physics of CRs and thermal plasma interaction are being correctly modeled. In Section 4, we investigate the acceleration of CRs in parallel shocks and the lack thereof in oblique shocks. Finally, in Section 5, we show a 3D simulation of an oblique, low Mach number shock with parameters comparable to the Earth’s bow shock, which exhibits features consistent with very recent *in-situ* observations.

## 2. HYBRID AND `dHybridR`

In the hybrid model the ion distribution function is approximated by a large number of *macro-particles* whose motion in phase space is determined by the Lorentz force. For a given set of electromagnetic fields, the macro-particle position and velocity can be advanced in time. The updated positions and velocities can be interpolated onto a grid, returns a fluid density and bulk flow; note that because the electrons are taken to be massless, they do not contribute to the bulk flow.

The electric field  $\mathbf{E}$  can be determined from the fluid electron momentum equation neglecting the electron inertia term (i.e., Ohm’s Law):

$$\mathbf{E} = -\frac{\mathbf{V}_e}{c} \times \mathbf{B} + \frac{1}{en} \nabla P_e \quad (1)$$

$$= -\frac{\mathbf{V}_i}{c} \times \mathbf{B} + \frac{\mathbf{J}}{enc} \times \mathbf{B} + \frac{1}{en} \nabla P_e \quad (2)$$

where  $\mathbf{B}$  is the magnetic field,  $\mathbf{V}_i$  and  $\mathbf{V}_e$  are the ion and electron bulk flows,  $n = n_i = n_e$  is the number density,  $\mathbf{J} = en(\mathbf{V}_i - \mathbf{V}_e)$  is the current and  $P_e$  is the (isotropic) electron pressure. The next assumption required for the hybrid model is to neglect the displacement current in Ampère’s law (i.e., the time derivative of the electric

field) such that  $\nabla \times \mathbf{B} = \frac{4\pi}{c} \mathbf{J}$ , this is the radiation-free limit, or the *Darwin approximation*. Finally, the electron pressure is prescribed by an equation of state, often taken as isotropic and polytropic. This electric field can then be used in Faraday’s law to update the magnetic field and thus yielding a self-consistent set of equations describing the evolution of the systems.

While the behavior of the ions is self-consistent in the hybrid model, the electrons physical description and evolution is more *ad hoc*. This is evident in choosing the most physically appropriate value of  $\gamma_{\text{eff}}$  for a polytropic electron equation of state,  $P_e \propto n^{\gamma_{\text{eff}}}$ . It could be argued that the electrons should be adiabatic and so  $\gamma_{\text{eff}} = 5/3$ . However, if the adiabatic description is used in shocks with a large Mach number, electrons cannot increase their entropy at the shock and the downstream electron pressure may end up being orders of magnitude smaller than the ion pressure. If one asserts that the electron and ion downstream pressure should be in equipartition, the Rankine-Hugoniot jump condition may be used to calculate what  $\gamma_{\text{eff}}$  should be (see the appendix of Caprioli et al. 2018, for more details). More complicated, anisotropic, prescriptions may be needed when dealing with magnetic reconnection (e.g., Le et al. 2009). In this work we will use the equipartition equation of state for shock simulations and the adiabatic one for CR streaming simulations.

Along with the disparate length and time scales, plasma systems can also span multiple scales in velocity space, ranging from thermal particles that make up the bulk of the plasma to CRs with kinetic energies orders of magnitude larger than their rest mass. An implicit assumption of the Darwin model is that the bulk velocities of the system are small relative to the speed of light, and because of this hybrid codes have traditionally not included relativistic effects for the macro-particle ions. However, since this approximation is based on *bulk motions* being small relative to the speed of light, even plasma systems with a non-relativistic background and a small number of relativistic particles (or CRs) can be modeled in this limit. This can be seen from a scaling argument of Ampère’s law with Maxwell’s correction:

$$\nabla \times \mathbf{B} = \frac{4\pi}{c} \mathbf{J} + \frac{1}{c} \frac{\partial \mathbf{E}}{\partial t} \rightarrow \frac{B}{\lambda} : \frac{4\pi J}{c} : \frac{E}{c\tau} \quad (3)$$

where derivatives have been replaced by  $\lambda$  and  $\tau$ , which correspond to characteristic length and time scales of the systems we are interested in studying, and the colon ( $:$ ) denotes an order of magnitude comparison. We can see from the scaling of Faraday’s law that  $E/B \sim V/c$ , where  $V = \lambda/\tau$  is the characteristic velocity of the system. Using this and that  $J \sim enV$  we can simplify our

scaling equation to

$$1: \frac{\lambda}{d_i} \frac{V}{v_A} : \left( \frac{V}{c} \right)^2 \quad (4)$$

where  $d_i = c/\omega_{pi} = \sqrt{c^2 m_i / 4\pi n e^2}$  is the ion inertial length (skin depth) and  $v_A = B/\sqrt{4\pi m_i n}$  is the Alfvén speed. Neglecting the displacement current is no longer appropriate when the third term becomes comparable to the other two and so we find that this approximation is good as long as

$$\left( \frac{V}{c} \right)^2 \ll 1, \text{ and } \frac{V v_A}{c^2} \ll 1 \quad (5)$$

where we used 1 for  $\lambda/d_i$ , which is the strictest value that can be used for hybrid simulations. The systems that we aim to study are composed of a background ion thermal population with number density  $n_i$ , characteristic velocity  $V_{\text{bkg}} \ll c$  and a high-energy CR population with  $n_{\text{cr}} \ll n_i$  and  $v_{\text{cr}} \sim c$ . The composite background + CR populations bulk flow (i.e., the characteristic flow) can be estimated as

$$\frac{V}{c} = \frac{n_i V_{\text{bkg}} + n_{\text{cr}} c}{c(n_i + n_{\text{cr}})} \approx \frac{V_{\text{bkg}}}{c} + \frac{n_{\text{cr}}}{n_i} \quad (6)$$

From this, we find three conditions the systems must meet for this approximation to be valid: 1)  $V_{\text{bkg}} \ll c$ , i.e., the system can not have relativistic flows; 2)  $n_{\text{cr}} \ll n_i$ , i.e., the CR number density must be negligible relative to the gas number density; 3)  $v_A \ll c$ , i.e., magnetic field energy density must be much smaller than the rest mass energy density. These conditions are satisfied for many systems in space and astrophysical plasmas where CR acceleration, transport and scattering are important.

To study these types of problems we have developed dHybridR, a hybrid simulation code that retains the fully relativistic ion dynamics. dHybridR is a generalization of the *dHybrid* code (Gargaté et al. 2007), where the relativistic Lorentz force is used for the ion macro-particle evolution, i.e.,

$$m_i \frac{d\gamma \mathbf{v}}{dt} = q\mathbf{E} + \frac{q\mathbf{v}}{c} \times \mathbf{B} \quad (7)$$

where  $\gamma$  is the Lorentz factor of a given macro-particle and given by  $\gamma = 1/\sqrt{1 - (v/c)^2}$ . This is implemented in the code using the well documented relativistic Boris algorithm (see Birdsall & Langdon 1991, for details).

The equations that govern both the electromagnetic fields and the particle dynamics are normalized to arbitrary magnetic field,  $B_0$ , and number density,  $n_0$ . Lengths are scaled to the ion inertial length based on this

density,  $L_0 \equiv d_{i0} = c/\omega_{pi0}$ , and time to the inverse ion gyro-frequency based on this magnetic field,  $t_0 \equiv \Omega_{ci0}^{-1} = \frac{cm_i}{eB_0}$ . Velocities are normalized to the ratio of the length and time normalizations and so a velocity of unity corresponds to the Alfvén speed in the reference magnetic field and density,  $v_0 \equiv L_0/t_0 = B_0/\sqrt{4\pi m_i n_0}$ . Electric fields are normalized to  $B_0 v_0/c$  and temperatures and energies to  $m_i v_0^2$ . Throughout this work simulations are initialized such that the unshocked/background plasma have a magnetic field, density and ion/electron temperature of unity and so the simulation units are effectively normalized to the background/upstream plasma parameters, i.e.,  $v_0 = v_A = v_{th}$  and  $d_{i0} = d_i = c/\omega_{pi} = r_{g,th}$ , the gyroradius of the thermal ions. By normalizing the discretized equations in this way, the speed of light only appears as the ratio  $c/v_0$  and then only occurs in the Lorentz factor,  $\gamma(v) = 1/\sqrt{1 - (v/v_A)^2 (v_A/c)^2}$ , in the Lorentz force equation.

The remainder of this paper is dedicated to the demonstration and validation of dHybridR simulating CR generation and transport for selected plasma systems, in which a small number of highly-energetic ions affects the dynamics. We will examine the non-resonant streaming instability (commonly referred to as the Bell instability), the resonant streaming instability, and different regimes of collisionless shocks.

In particular, we will study the transition from non-relativistic to relativistic CR energies in fast non-relativistic shocks; since the required timestep is inversely proportional to  $c/v_A$ , we initially focus on shock environments where  $v_A$  is rather large, such as radio supernovae, where  $V_{\text{sh}} \sim 0.1c$ ,  $B_0 \sim 0.1G$  and  $n_0 \sim 10^3 \text{cm}^{-3}$  at the peak of the synchrotron emission (e.g., Chevalier & Fransson 2006). These parameters correspond to Alfvénic mach numbers  $M_A \equiv V_{\text{sh}}/v_A \sim 10$  and  $c/v_A \sim 100$ . Then, we show simulations of lower-Mach number shocks with rather large  $c/v_A$ , which are well suited for studying heliospheric systems, such as planetary bow shocks and interplanetary shocks triggered by coronal mass ejections.

There are numerous astrophysical systems where  $c/v_A$  and  $c/v_{\text{sh}}$  are considerably larger than the simulations presented in this work; however, as long as there is a clear separation of scales between the thermal/Alfvénic speed, the speed of the shock, and the speed of light, the underlying physics can be studied fruitfully. This idea implies that the physical results from these simulations, and dHybridR in general, are potentially applicable to many different astrophysical systems such as shocks from supernova remnants.

### 3. RESONANT AND NON-RESONANT STREAMING INSTABILITY

To verify that dHybridR correctly simulates the physics relevant to systems with CRs, we present two simulations in which the non-resonant (Bell 2004) and resonant (e.g., Kulsrud & Pearce 1969; Skilling 1975a) CR streaming instabilities are excited. In both cases, low density relativistic CRs affect the non-relativistic background plasma by amplifying magnetic fluctuations. Because of this coupling between CRs, magnetic fields, and thermal background plasma, these serve well as test cases for dHybridR.

The two simulations have quasi-1D periodic domains of size  $[L_x, L_y] = [10^4, 5]d_i$  with a uniform magnetic field  $\mathbf{B} = B_0\mathbf{x}$  and a stationary background population of protons (technically, ions with a charge to mass ratio equal to protons) with thermal speed equal to  $v_A$ , corresponding to a plasma beta of  $\beta_i = P_i/P_B = 8\pi nT_i/B^2 = 2$ , where  $P_i$  and  $P_B$  are the ion and magnetic pressures. Superimposed on the background population is a lower-density CR population with a power-law distribution in momentum space  $f(p) \propto p^{-4}$  extending from  $p_{\min}/m_i c = 1$  to  $p_{\max}/m_i c = 10^4$ , which is isotropic in a frame moving with a drift velocity  $v_d = 10v_A$ . In both simulations, the speed of light is set to be  $c = 100v_A$  and there are two grid cells per  $d_i$ ; with 100 and 4 macro-particles per cell are used for the background and CR populations, respectively. The CR number density relative to the background population is adjusted to trigger either the non-resonant ( $n_{\text{cr}}/n_i = 10^{-2}$ ) or the resonant ( $n_{\text{cr}}/n_i = 10^{-4}$ ) instability (Bell 2004; Amato & Blasi 2009). The time step is chosen to be  $dt = 2.5 \times 10^{-3}\Omega_{ci}^{-1}$  based on the initial magnetic field.

The magnitude of the CR current controls which instability has the largest growth rate. More precisely, following Amato & Blasi (2009) we introduce the parameter

$$\bar{\sigma} \equiv \frac{4\pi r_L}{c} J = \frac{n_{\text{cr}} p_{\min} v_d}{n_i m_i v_A^2}, \quad (8)$$

where  $r_L$  is the gyro-radius of the particles with the minimum momentum in the CR distribution,  $p_{\min}$ .  $J$  is the CR current  $J = en_{\text{cr}}v_d$  where  $n_{\text{cr}}$  is the CR number density and  $v_d$  is the bulk/drift velocity of the CR distribution. For values of  $\bar{\sigma} \gg 1$  the non-resonant mode's growth rate becomes dominant. If  $\bar{\sigma} \ll 1$  the growth of the non-resonant mode is suppressed, and the resonant mode becomes dominant (Bell 2004; Amato & Blasi 2009). For  $n_{\text{cr}}/n_i = 10^{-2}$  and  $n_{\text{cr}}/n_i = 10^{-4}$ , Equation 8 yields  $\bar{\sigma} = 10$  and 0.1, which will preferentially excite the non-resonant and resonant instabilities, respectively. Testing both the strong and the weak current regimes

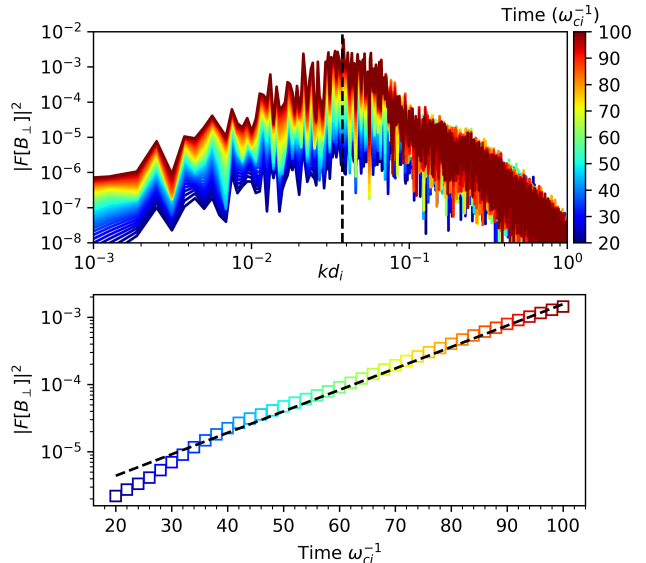


**Figure 1.** Perpendicular magnetic energy spectrum,  $|F_{\perp}|^2$ , as a function of wave number  $k$  and time for a 1D simulation of the non-resonant streaming instability. Top panel: spectrum as a function of  $kd_i$ , where each color corresponds to a different time in the simulation; the vertical black dashed line corresponds to the  $k_{\max}$  predicted by the linear theory (Equation 9). Bottom panel:  $|F_{\perp}|^2(k = k_{\max})$  as a function of time, compared with the growth rate predicted by linear theory (dashed line).

allows us to probe both MHD-like and purely kinetic physics. The theory of these instabilities and the transition between the two has been detailed in Amato & Blasi (2009) for a  $\propto p^{-4}$  CR distribution, and we compare such a linear theory with simulations.

For the non-resonant (or Bell) regime the fastest growing mode,  $k_{\max}$ , and its corresponding growth rate,  $\gamma_{\max}$ , read:

$$k_{\max}d_i = \frac{\gamma_{\max}}{\Omega_{ci}} = \frac{1}{2} \frac{n_{\text{cr}} v_d}{n_i v_A}, \quad (9)$$

(Bell 2004). Instead, in the resonant regime we have

$$k_{\max}d_i = \frac{m_i v_A}{p_0}; \quad \frac{\gamma_{\max}}{\Omega_{ci}} = \frac{\pi}{8} \frac{n_{\text{cr}} v_d}{n_i v_A}, \quad (10)$$

where Equation 10 is calculated by Taylor-expanding equation 28 in Amato & Blasi (2009) in terms of  $n_{\text{cr}}v_d p_0/n_i m_i v_A^2$  and keeping only the linear term.

To compare these predictions with the simulation, we compute the magnetic power spectrum of the perpendicular magnetic field ( $|F_{\perp}|^2 = |\text{FFT}[B_y]|^2 + |\text{FFT}[B_z]|^2$ , where FFT is the discrete fast Fourier transform calculated along the  $x$  direction) at different times throughout the simulation. This quantity can be seen in the first panel of Figure 1 and Figure 2 for the non-resonant and resonant cases respectively. In both of

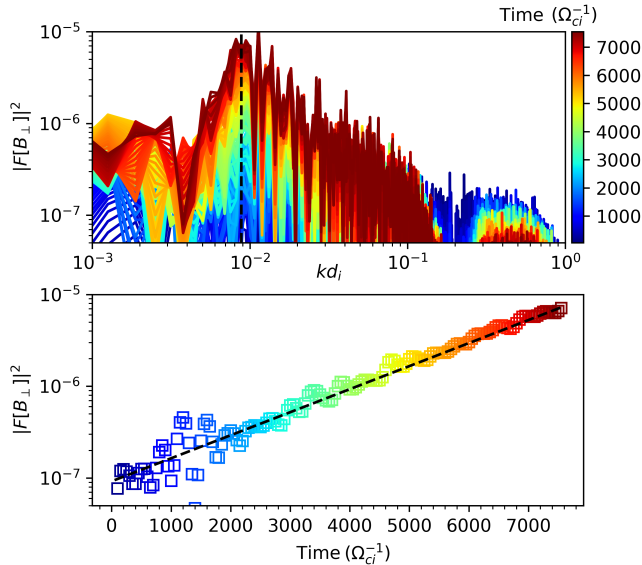


**Figure 2.** As in Figure 1 for a 1D simulation of the resonant streaming instability. The theoretical expectations are from Equation 10.

these figures the color corresponds to different times in the simulation and the black dashed line shows  $k_{\max}$  predicted by Eq.9 and 10. The agreement for the maximum growth rate between theory and simulations is excellent.

The second panels of Figure 1 and Figure 2 show the value of  $|F[B_{\perp}]|^2$  at  $k_{\max}$  as a function of time. The magnetic energy should increase exponentially in time as  $|F[B_{\perp}]|^2 \propto e^{2\gamma_{\max}t}$  and the black dashed line corresponds to the  $\gamma_{\max}$  given by Equation 9 and 10; there is a remarkable agreement between theory and simulations in both the non-resonant and resonant cases.

It is worth noting the differences in the time and length scales of the two instabilities simulated. The resonant instability stems out from a gyro-resonant interaction with the CR population (e.g., Kulsrud & Pearce 1969; Skilling 1975a; Bell 1978; Zweibel 2003) and amplifies magnetic fluctuations on scales comparable to the CR gyroradius. Since  $\bar{\sigma}$  must be small for the resonant instability, it is clear from Equation 10 that the growth rates are small compared to the cyclotron frequency of the background population.

This is evident in Figure 2, where the simulation was run for almost  $10^4 \Omega_{ci}^{-1}$  and the power in modes with wavelengths near  $10^3 d_i$  increased by two orders of magnitude. The non-resonant simulation, in contrast, occurs due to a near gyro-resonance with the background ion population (e.g., Weidl et al. 2019) and amplifies fluctuations with smaller wavelengths with a growth rate that is two orders of magnitude larger. The agreement between simulations and the linear theory verifies that

Run	$M$	$c/V_A$	$L_x/d_i$	$L_{\perp}/d_i$	$\Delta x/d_i$	$\Delta t \Omega_{ci}$	$\vartheta_{Bn}^{\circ}$
A	20	200	$8 \times 10^5$	200	0.5	.0025	0
B	15	50	$10^5$	150	0.5	.005	0
C	30	10000	$10^4$	2700	0.5	.0025	70
3D	5	100	1000	100	0.5	.02	70

**Table 1.** Parameters for the shock simulations presented in this work. From left to right: Alfvénic mach number (i.e.,  $v_{sh}/V_A$ ), speed of light, longitudinal ( $L_x$ ) and transverse ( $L_{\perp}$ ) box sizes, spacial grid resolution, time step and angle of the initial magnetic field relative to the upstream plasma bulk flow. Note, the time step in simulations C and 3D are set by the speed of fastest particles in the simulation, not the speed of light.

dHybridR can accurately model the physical coupling of the thermal background plasma and a drifting CR population for quasi-linear problems, both in the strong and weak current regimes.

## 4. NON-RELATIVISTIC SHOCKS

### 4.1. Setup and Simulation Parameters

Shock simulations were performed with dHybridR following the set up described in Gargaté & Spitkovsky (2012). The simulations are performed in 2.5D (2D in real space, and 3D in momentum space) on a regular Cartesian grid, with periodic boundary conditions in the  $y$  direction (transverse to the shock), open on the right boundary ( $+x$  direction or normal and upstream of the shock), and reflecting on the left boundary ( $-x$  direction and downstream of the shock). The shock is formed by initializing the plasma with a bulk flow in the  $-x$  direction; the plasma closest to the left wall is reflected and begins streaming in the  $+x$  direction. This configuration is unstable and within  $\sim 10 \Omega_{ci}^{-1}$  a shock forms and travels upstream. Across the shock fluid quantities satisfy the Rankine–Hugoniot (RH) jump conditions. For the simulations in this study, the initial/upstream magnetic field and density are set to unity and the initial magnetic field points in the first quadrant of the  $x, y$  plane, the shock angle is measured relative to the positive  $x$  direction (normal to the shock)  $\vartheta_{Bn}$  (e.g., for a parallel shock  $\mathbf{B} = B_0 \hat{\mathbf{x}}$  and  $\vartheta_{Bn} = 0$ ). The initial ion thermal velocity is equal to the upstream Alfvén speed and the electron temperature is equal to the ion temperature ( $T_0 = T_i = T_e$ ). Following previous hybrid shock simulations (e.g., Gargaté & Spitkovsky 2012; Caprioli & Spitkovsky 2014a), a polytropic index for the electron equation of state is selected so that the downstream electron thermal energy will be half of the upstream kinetic energy in the shock frame (also see Caprioli et al. 2018, for more details).

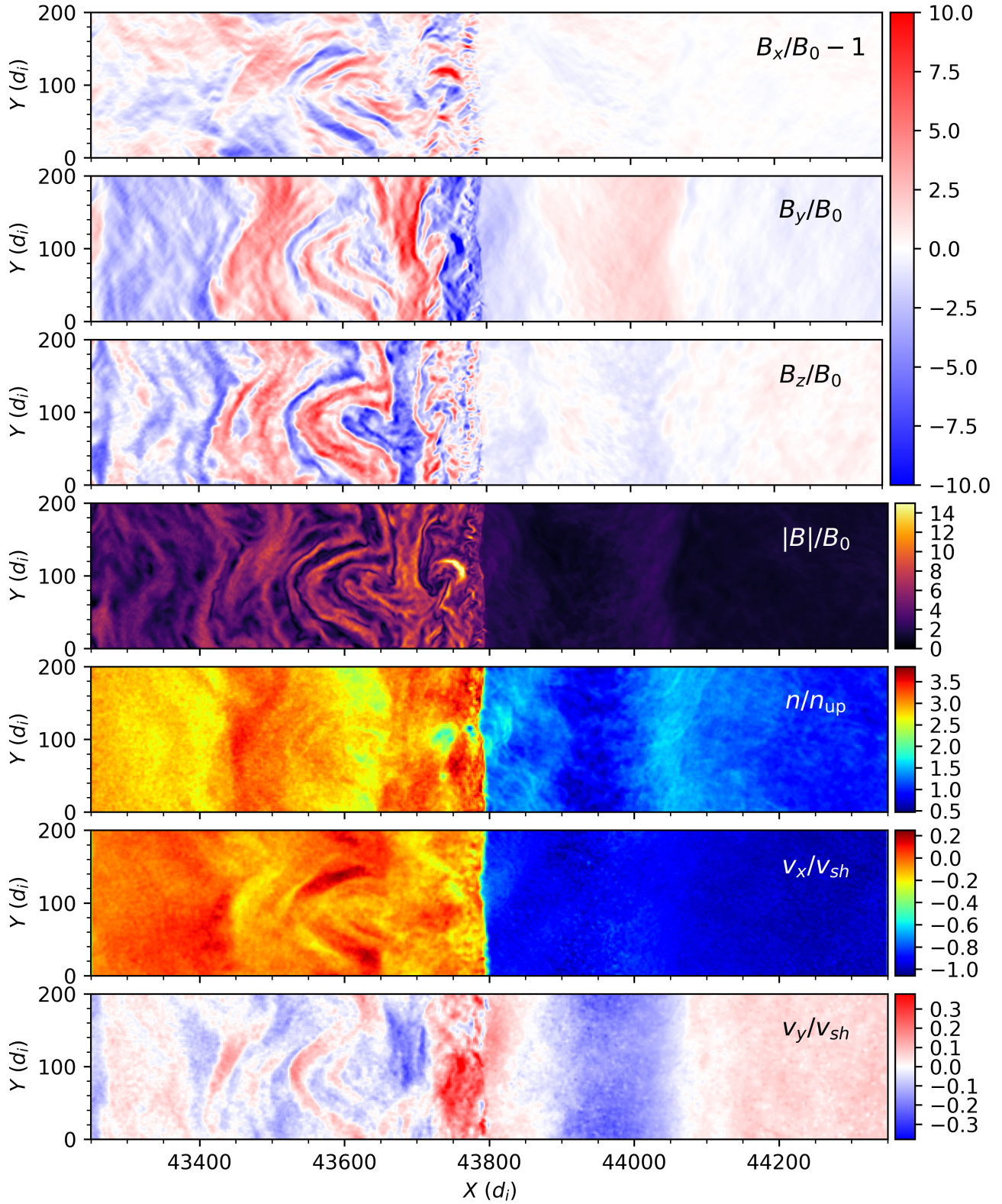


**Figure 3.** 2D plasma/fluid quantities around the shock at  $t = 5560\Omega_{ci}^{-1}$  from Run A in Table 1. From top to bottom: the 3 components (x,y and z) of the magnetic field in excess to the background ( $\mathbf{B} - \mathbf{B}_0$ ), magnitude of the magnetic field, density, normal (x) transverse (y) bulk flow. All of the quantities are normalized to the upstream values.

Shocks are parametrized by their Alfvénic and sonic Mach numbers,  $M_A = v_{\text{sh}}/v_A$  and  $M_s = v_{\text{sh}}/v_s = v_{\text{sh}}/\sqrt{2\gamma k_B T_0/m_i}$ , where  $v_{\text{sh}}$  is the upstream velocity in the lab/simulation frame (i.e., in the frame where the downstream medium is at rest). The choice of temperature in these simulations links the two Mach numbers,  $M_A = \sqrt{10/3}M_s$  and in this work we will reference the Mach number as simply  $M \equiv M_A \simeq M_s$ . We use 2 grid cells per  $d_i$  and 4 particles per cell.

Simulations were run for thousands of cyclotron times to model the CRs transition from non-relativistic to relativistic energies. The largest and longest run of these simulations is shown in Figure 3 at the end of the simulation, which shows various plasma/fluid quantities around the shock. For this run we used  $M = 20$ ,  $c = 200V_{A0}$  and  $[L_x, L_y] = [8 \times 10^5, 200]d_{i0}$ , with the time step determined by the Courant-Friedrichs-Lewy condition based on the speed of light. These parameters allowed us to run unprecedentedly-long hybrid simulations of non-relativistic shocks, up to  $\sim 6000\Omega_{ci}^{-1}$  before the highest-energy CRs began to escape from the box.

#### 4.2. Momentum and Energy

Consistent with results from previous non-relativistic hybrid simulations of parallel shocks (e.g., Giacalone et al. 1997; Burgess et al. 2012; Caprioli & Spitkovsky 2014a,b,c), we find that thermal ions can be spontaneously energized into an extended power-law distribution. Figure 4 shows the post-shock distribution function as a function of both the ion velocity normalized to  $c$  (first panel) and the ion momentum normalized  $m_i c$  (the second panel). The majority of ions are thermally heated by the shock, forming the Gaussian peak around  $p/m_i \sim v \sim 0.1c$ ; the black dashed lines correspond to a Gaussian with temperature reduced by 20% with respect to the one predicted by the RH conditions for a mono-atomic ideal gas. The deviation from the prediction is consistent with the amount of energy (about 10 – 20% of the shock ram energy) that is channeled in the non-thermal power-law distribution that develops beyond  $v \sim 0.2c$ , whose extent increases with time (color code). The velocity spectra cuts off at  $v < c$  as expected, however the momentum continues to extend with the same slope beyond  $p \gtrsim m_i c$ . The distributions shown in Figure 4 are multiplied by  $v^{-4}$  and  $p^{-4}$ , respectively.

While the momentum spectra shows a nearly constant power law slope, the energy spectrum should have different slopes in the non-relativistic and relativistic regimes. The energy distribution is linked to the momentum distribution through the conservation of the phase-space volume:  $f(E) = 4\pi p^2 f(p) dp/dE$ . In the

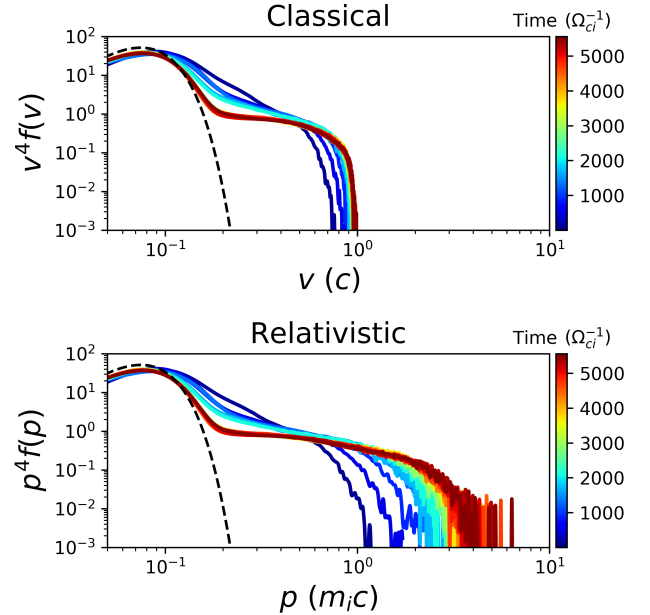


**Figure 4.** Velocity and momentum spectra calculated downstream of the shock (top and bottom panels) for Run A. Different colors correspond to different times in simulation as detailed by the color bars. Velocity and momentum are normalized by  $c$  and  $m_i c$ , and spectra are multiplied by  $v^4$  and  $p^4$ , respectively, for comparison with the standard DSA prediction. The black dashed line shows a Gaussian with temperature  $\sim 20\%$  lower than the temperature predicted by the RH conditions, which compensates for the energy that goes into accelerated ions in the power-law tail.

non-relativistic regime,  $E \propto p^2$  and so for a momentum power-law index of  $q$ , the energy distribution should go as  $f(E) \propto E^{(1-q)/2}$ , i.e.,  $E^{-1.5}$  for  $q = 4$ . In the relativistic regime,  $E \propto p$  and thus the kinetic energy distribution should scale as  $f(E) \propto E^{2-q}$ , i.e., the canonical  $E^{-2}$  for  $q = 4$ .

The energy spectrum for our benchmark simulation is shown in Figure 5, where the spectrum is multiplied by  $E^{1.5}$  in the top panel and  $E^2$  in the bottom panel in an attempt to emphasize the agreement with the expected slopes in both the non-relativistic and the relativistic regimes. In this run some particles became relativistic, with  $\gamma \gtrsim 5$ , but running such a large simulation long enough for the power-law tail to extend beyond  $\sim 10m_i c^2$  is computationally impractical. Thus, in order to see the transition in the energy power-law slope more clearly, we performed a simulation with a smaller speed of light relative to the shock velocity and Alfvén speed (Run B in Table 1); the reduced separation of scales allows us to investigate the trans-relativistic regime more easily. Figure 6 shows the momentum and energy distribution for Run B at  $t = 2000\Omega_{ci}^{-1}$  (top and bottom pan-

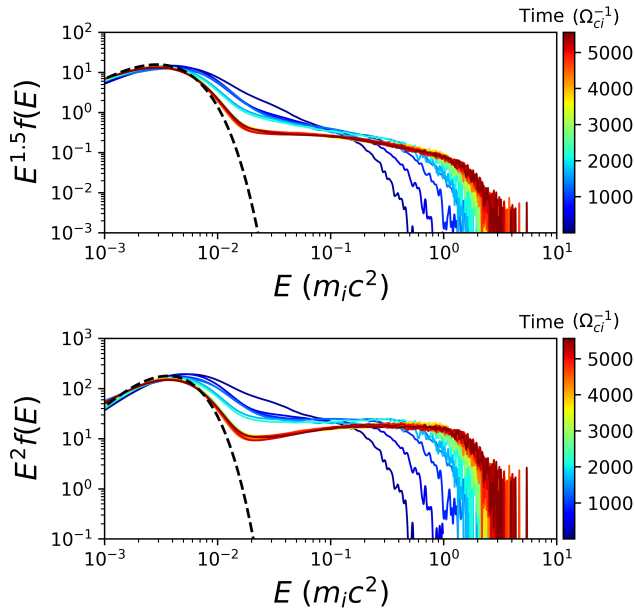


**Figure 5.** Post-shock spectra as a function of the kinetic energy spectrum normalized to  $m_i c^2$  (i.e.,  $\gamma - 1$ ) for Run A in time. Distributions are multiplied by  $E^q$ , where  $q$  is the expected power law in the non-relativistic ( $E^{1.5}$ ) and relativistic ( $E^2$ ) regimes (top and bottom panels, respectively).

els, respectively). In the first panel the distribution is fitted with to a power-law  $\propto p^{-4}$  multiplied by an exponential cut off at  $p_{\max} = 9m_i c$ . The bottom panel, shows the energy distribution, multiplied by  $E^2$ ; the black and red dashed lines correspond to the relativistic and classical power-law predictions based on the fit curve from the top panel. In essence, the black line shows the shape of the distribution if  $E = m_i c^2 (\sqrt{p^2/c^2 + 1} - 1)$  and the red line for  $E = p^2/2m_i$ . In the non-relativistic regime, both the black and red predictions agree well with the measured spectrum; as the distribution extends into the relativistic regime ( $E \gtrsim 2m_i c$ ), though, there is a clear steepening to the slope of  $-2$ , followed by the exponential cutoff, which agrees well with the black line prediction. The classical prediction (red line), however, continues to increase for nearly an order of magnitude in energy beyond the actual energy cut-off.

This analysis shows, for the first time in hybrid simulations, how non-relativistic shocks can accelerate particles to ultra-relativistic energies (with Lorentz factors up to  $\gamma \gtrsim 20$  in our case), also confirming that DSA produces power-laws *in momentum space* across the non-relativistic and relativistic regimes. These results are consistent with those obtained for both electrons and ions in 1D full-PIC simulations of non-relativistic shocks (Park et al. 2015) and for electrons in full-PIC simulations of trans-relativistic shocks (Crumley et al. 2019).

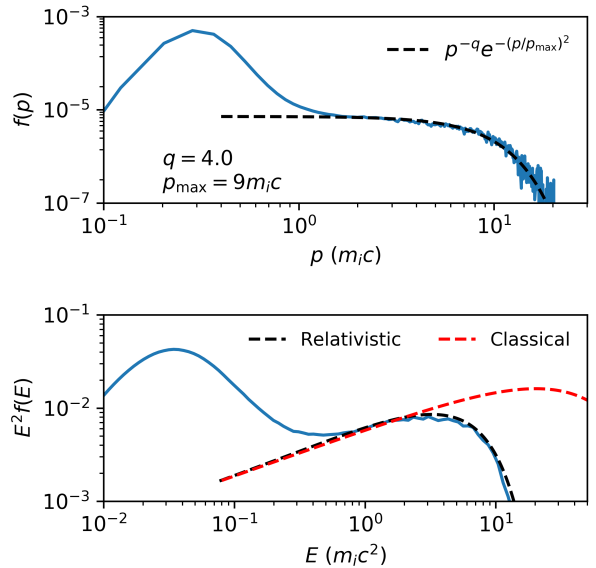


**Figure 6.** Post-shock momentum and energy distributions in Run B at  $t = 2000\Omega_{ci}^{-1}$  (top and bottom panels, respectively). The high-momentum tail is well fitted by a distribution  $f(p) \propto p^{-q} \exp(-p/p_{\max})^2$  with  $q = 4$  and  $p_{\max} = 8m_i c$ . Such a fitting curve is converted to an energy fitting using either the classical ( $E = p^2/2m_i$ , red line) or the relativistic ( $E = m_i c^2 (\sqrt{p^2/c^2 + 1} - 1)$ , black line) scalings. The energy distribution is multiplied by  $E^2$  to emphasize the transition from  $E^{-1.5}$  to  $E^{-2}$ .

One important astrophysical application that stems put from these preliminary runs is relevant for young SNe. In fact, if we consider the typical values for the magnetic field inferred in type Ib & Ic supernova with Wolf-Rayet star progenitors (Chevalier & Fransson 2006), the inverse cyclotron time  $\Omega_{ci}^{-1}$  would be on the order of milliseconds. Both the A & B Runs have  $M_A$  and  $c/v_A$  typical of these systems and so physically these simulations are modeling a few seconds of fast radio SNe. Notably, in these simulations, thermal protons are accelerated to multi-GeV energies in a matter of seconds, which has implications for the generation of  $\gamma$ -rays and neutrinos, as discussed below.

#### 4.3. Rate of Maximum Energy Increase

An important question regarding DSA is what is the maximum energy,  $E_{\max}(t)$ , of the particles produced by a shock with a given speed and magnetic field in a finite amount of time (e.g., O’C. Drury 1983; Lagage & Cesarsky 1983a; Blasi et al. 2007). When the magnetic field perturbations responsible for particle diffusion is self-generated by the CRs,  $E_{\max}$  is determined by the current in CRs streaming in the upstream medium,  $J_{\text{cr}}$ ; such a current can be estimated as the number density  $n_{\text{cr}}$  of particles close to the instantaneous  $E_{\max}$ ,

times their velocity,  $v_{\text{cr}}$ . For a momentum spectrum  $f(p) \propto p^{-4}$ , in the non-relativistic regime, one has  $n_{\text{cr}} \propto p_{\text{max}}^3 f(p) \propto E_{\text{max}}^{-1/2}$  and  $v_{\text{cr}} \propto E_{\text{max}}^{1/2}$ , so that  $J_{\text{cr}} = en_{\text{cr}}v_{\text{cr}} \simeq$  is constant in time. Conversely, in the relativistic regime  $n_{\text{cr}} \propto E_{\text{max}}^{-1}$  and  $v_{\text{cr}} \simeq c$ , so that  $J_{\text{cr}} \propto E_{\text{max}}^{-1}$ ; therefore, the current decreases when the maximum CR energy increases and one may expect a slower amplification of the magnetic field, and in turn a slower rate of increase of  $E_{\text{max}}$ . Note that this effect may be partially compensated by the fact that the CR precursor becomes larger when  $E_{\text{max}}$  increases, so that the time available for growing the field (of the order of one advection time on a CR diffusion length) also increases. The net effect in general depends on whether most of the field growth is provided by escaping or diffusing particles, and on the details of the instability saturation (Caprioli & Spitkovsky 2014b).

Bai et al. (2015) found that the rate of increase of  $E_{\text{max}}$  decreases when CRs become relativistic, but in MHD-PIC simulations ion injection is prescribed by hand, which makes it impossible to study the back-reaction of relativistic CRs self-consistently.

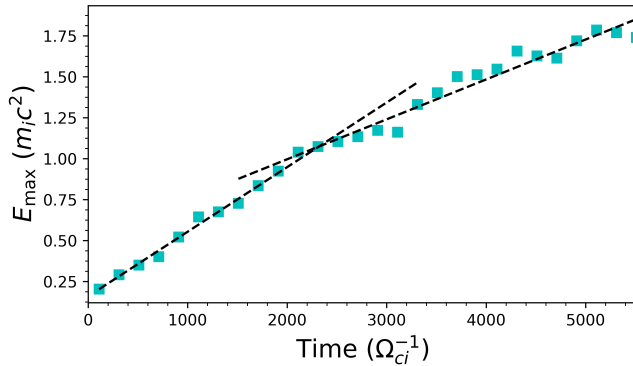


**Figure 7.** Evolution of the maximum CR energy (Equation 11, in units of  $m_i c^2$ ) for Run A in Table 1.

To quantify the change in the maximum energy we define  $E_{\text{max}}$  as the exponential cutoff of the CR distribution, taken in the form  $f(E) \sim E^{-q} e^{-E/E_{\text{max}}}$ . Following Bai et al. (2015), we calculate  $E_{\text{max}}$  by integrating over the energy distribution function:

$$E_{\text{max}} \sim \frac{\int E^4 f(E) dE}{\int E^3 f(E) dE}. \quad (11)$$

Since  $f(E)$  has an energy slope between 1.5 and 2, the integral differs from  $E_{\text{max}}$  by a constant of order unity. Figure 7 shows the maximum energy as a function of time for Run A, where  $E_{\text{max}}(t) \propto t$  can be fitted with a broken linear function with a change of slope in the

trans-relativistic regime. The rate of increase of  $E_{\text{max}}$  is about  $3.9 \times 10^{-4} m_i c^2 \Omega_{ci}$  and  $2.4 \times 10^{-4} m_i c^2 \Omega_{ci}$  below and above the rest mass energy, respectively.

The connection between the self-generated diffusion and the growth of the maximum CR energy can be made more explicit by measuring the average diffusion coefficient upstream of the shock. For DSA, the return time upstream is typically the bottleneck of the acceleration rate. Such a diffusion coefficient  $D(E)$  is estimated using the approach outlined in Caprioli & Spitkovsky (2014c), namely:

$$D(E) \simeq \frac{v_{\text{sh}}}{f_{\text{sh}}(E)} \int_{\text{shock}}^{x_0} f(x, E) dx \quad (12)$$

where  $x_0$  is a position far enough upstream that the CR population is negligible and  $f_{\text{sh}}(E)$  is the CR distribution function just downstream of the shock.

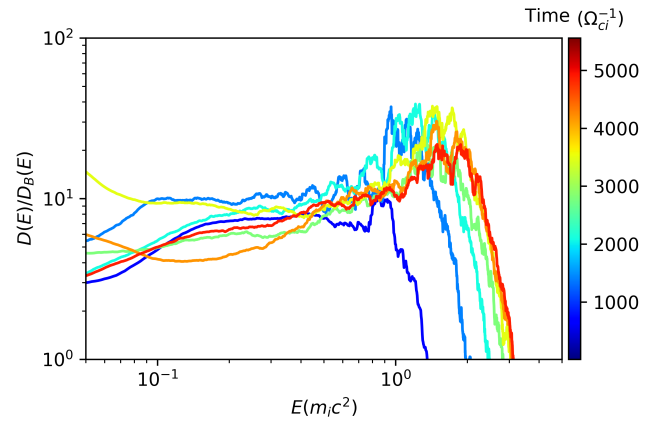


**Figure 8.** Effective diffusion coefficient (Equation 12) normalized to the Bohm diffusion coefficient as a function of energy for Run A in Table 1. The different color lines correspond to different times in the simulation.

Figure 8 shows the time evolution of the diffusion coefficient normalized to the Bohm diffusion coefficient ( $D_B \equiv vr_L/2$ ) for Run A. As discussed in (Caprioli & Spitkovsky 2014c), for  $M = 20$  the diffusion coefficient is about an order of magnitude larger than Bohm, which is consistent with having self-generated magnetic fluctuations—at scales resonant with the CRs—that are approximately an order of magnitude smaller than the initial upstream magnetic field. As the simulation evolves in time and the maximum energy transitions into the relativistic regime and we can see a change in the diffusion coefficient. We find the value of the diffusion coefficient is consistently larger at relativistic energies,  $D(m_i c^2) \sim 10 - 20 D_B$ , than at non-relativistic energies,  $D(m_i c^2/5) \sim 5 - 10 D_B$ . The rate of maximum CR energy increase for non-relativistic shocks can be written

as (Caprioli & Spitkovsky 2014c):

$$\frac{E_{\max}(t)}{\frac{1}{2}m_i v_{\text{sh}}^2} \approx \frac{1}{3} \frac{D_B(E_{\max})}{D(E_{\max})} \Omega_{ci} t. \quad (13)$$

The increase in the diffusion coefficient as CRs transition to relativistic energies is consistent with the reduction in the rate of change of  $E_{\max}$ , as seen in Figure 7. The increase of the diffusion coefficient by an approximate factor of 2 agrees with the reduction of the slope by a comparable factor.

In previous hybrid simulations, the self-generated diffusion coefficient normalized to the Bohm coefficient has been linked to the Mach number by  $D/D_B \propto 1/\sqrt{M}$  (Caprioli & Spitkovsky 2014b,c). Using this scaling along with the measured rate of increase of the maximum energy from our simulation, we can calculate a prediction for the maximum energy as a function of time:

$$\frac{E_{\max}}{\text{GeV}} \approx 20 \left( \beta_{\text{sh}}^5 \frac{n}{\text{cm}^{-3}} \frac{B}{\text{Gauss}} \right)^{1/2} \frac{t}{\text{s}} \quad (14)$$

where  $\beta_{\text{sh}} \equiv v_{\text{sh}}/c$ . Again, for the typical values of fast radio supernovae, with  $\beta_{\text{sh}} \gtrsim 0.01$ , CRs with GeV energies will be reached within seconds, and TeV CRs will be produced in about an hour. If the circumstellar medium is dense enough, multi-TeV neutrinos<sup>1</sup> in the range of sensitivity of Ice Cube could be produced in a matter of days after the SN explosion.

#### 4.4. Acceleration Efficiency

We consider the evolution of the fraction of shock energy that is transferred to CRs as a function of time. Following Caprioli & Spitkovsky (2014a) and Caprioli et al. (2015), we distinguish the CRs as the ions that achieved energies  $E \gtrsim 10E_{\text{sh}}$  and define the acceleration efficiency  $\varepsilon_{\text{cr}}$  as the fraction of the energy density in these particles normalized by the total energy density.

$$\varepsilon_{\text{cr}} = \frac{\int_{10E_{\text{sh}}}^{\infty} E f(E) dE}{\int_0^{\infty} E f(E) dE} \quad (15)$$

Figure 9 shows that an acceleration efficiency on the order of 10% is reached within the first hundred inverse cyclotron times, and then remains nearly constant throughout the entire simulation, consistent with what was seen in the non-relativistic case (Caprioli & Spitkovsky 2014a). The vertical black dashed line denotes when  $E_{\max} \sim m_i c^2$ , the color corresponds to  $E_{\max}/m_i c^2$  as shown in Figure 7.

<sup>1</sup> Hadronic neutrinos and  $\gamma$ -rays of energy  $E$  are produced by parent protons of energy  $\sim 10E$ .

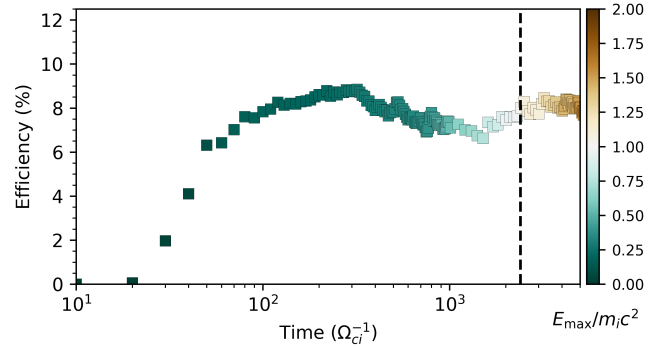


**Figure 9.** CR acceleration efficiency (fraction of energy in particles with  $E > 10E_{\text{sh}}$ ) as a function of time for Run A. The black dashed vertical line corresponds to when the highest energy particles become relativistic. The color of each point corresponds to  $E_{\max}/m_i c^2$  as shown in Figure 7.

From this it is clear that  $\varepsilon_{\text{cr}}$  is unaffected as the CR population transitions from non-relativistic to relativistic energies, and that the canonical value of  $\sim 10\%$  quoted by (Caprioli & Spitkovsky 2014a) should be considered the asymptotic one. In this respect, it is worth stressing that in the non-relativistic regime the efficiency  $\varepsilon_{\text{cr}} \propto E^2 f(E) \propto E^{1/2}$  is typically dominated by the highest-energy CRs, while in the relativistic regime there is about the same energy density per decade. Since  $\varepsilon_{\text{cr}}$  saturates well before CRs become trans-relativistic, it is necessary for the shock to “be aware” of the efficient CR acceleration; such a CR feedback will be discussed in greater detail in forthcoming works, but here we mention that the pressure in the CR precursor affects the dynamics shock front, which reacts by injecting fewer particles into DSA.

Until this moment we have not discussed oblique or perpendicular shocks. This is because it has previously been found in classical hybrid simulations that shocks with  $\vartheta_{Bn} \gtrsim 50^\circ$ , thermal ions are not energized enough to initiate the DSA process (Caprioli & Spitkovsky 2014a; Caprioli et al. 2015). Note that, if the injection issue is overcome, for instance when pre-energized CR seeds are present (Caprioli et al. 2018), or the presence of external plasma turbulence, acceleration at oblique shocks proceeds unhindered, even more rapidly than at quasi-parallel shocks (e.g., Jokipii 1987; Giacalone 2005).

Recently, PIC-MHD simulations of very oblique shocks ( $\vartheta_{Bn} \gtrsim 70^\circ$ ) have suggested that thermal particle injection and DSA will eventually occur for simulations run long enough van Marle et al. (2018). We have tested this claim with the full-hybrid dHybridR code and did not recover such a result. Figure 10 shows a

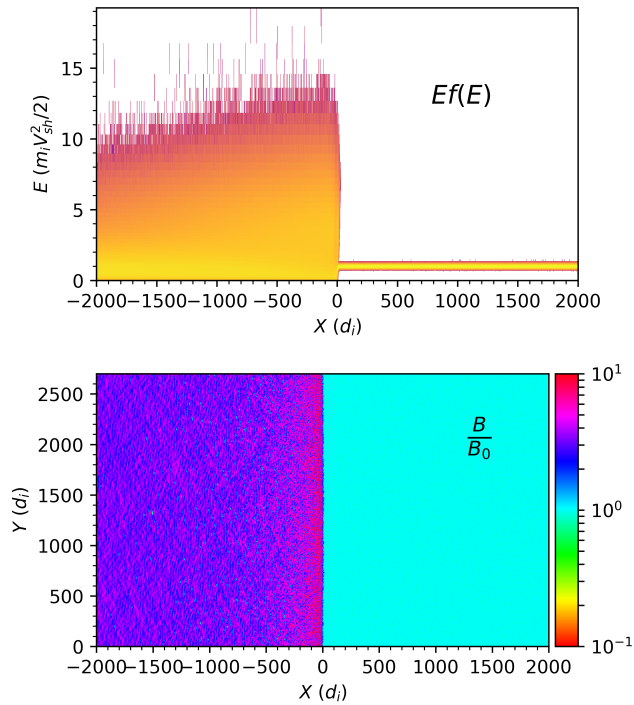


**Figure 10.** Quantities from the quasi-perpendicular shock simulation described by Run C in Table 1. Top panel: Energy spectrum at each position  $x$ ; Bottom panel: 2D plot of the magnitude of the magnetic field. There is no evidence of DSA and of magnetic field amplification upstream.

simulation perform with the same initial parameters as the quasi-perpendicular,  $M = 30$  simulation discussed in van Marle et al. (2018). The simulation is  $[L_x; L_\perp] = [10^4; 2.7 \times 10^3]d_{i0}$  in size with two cells per skin depth in each direction and was run for a comparable amount of time ( $600\Omega_{ci}^{-1}$ ). Using 4 particles per cell, the dHybridR simulation has approximately 172,800 macro particles per normal skin depth downstream of the shock (i.e., 172,800 macro-particles per area  $1d_i$  long by  $2700d_i$  wide), a statistics more than sufficient to test the acceleration efficiency claimed in the PIC-MHD simulation, which used only  $10^3$  CR particles per normal skin depth. The top panel shows the energy density distribution as a function of  $x$ , in which energy is normalized to the shock energy. Downstream of the shock ( $x < 0$ ), ions are heated up to supra-thermal energies ( $E \lesssim 10E_{sh}$ ), but there is no DSA tail, and no energetic particles upstream ( $x > 0$ ). The bottom panel of Figure 10 shows a 2D plot of the magnitude of the magnetic field, which reveals the canonical downstream compression, with additional some small-scale deviations (which we discuss below); the upstream magnetic field, instead, is unperturbed. These results stress how

a self-consistent model for ion injection can only be provided by full-hybrid simulations.

## 5. 3D SIMULATIONS

Finally, we present a smaller Mach number ( $M = 5$ ), quasi-perpendicular 3D shock simulation, identified as Run 3D in Table 1. This simulation was initialized with conditions that more closely match those typically observed at Earth’s bow shock, which is formed by the solar wind impinging on the Earth’s magnetosphere. dHybridR is well suited to study low-Mach-number heliospheric shocks because in this systems ions are typically accelerated only to trans-relativistic energies, and because the relevant sizes and scales can be modeled inch for inch at a reasonable computational cost. In Fig 11 we present an orthographic projection of  $B_z$ , where  $z$  is the direction normal to the upstream flow and the mean upstream magnetic field; therefore,  $B_z$  is the self-generated component of the magnetic field. Upstream of the shock there are no indications of magnetic field amplification, in agreement with the 2D simulation. However, downstream some magnetic structures can be observed: there is a clear rippling of the magnetic field along the shock interface, which is produced by shock reformation, consistent with what has been previously found in observations (Johlander et al. 2016, 2018) and simulations (Lowe & Burgess 2003; Caprioli et al. 2015; Burgess et al. 2016).

The black line in Figure 11 represents the trajectory of a synthetic probe through the simulation box, mimicking in-situ spacecraft observations, and Figure 12 shows the magnetic field measured by such a probe. The trajectory is diagonal through the shock interface, with only a small component normal to the upstream magnetic field ( $0.681\hat{x} + 0.727\hat{y} - 0.091\hat{z}$  intersecting a point in the middle of the  $y-z$  plane at  $x = 312.5d_i$ ). From this cut, the periodic structure of the ripples can be clearly seen; considering that the direction of propagation is primarily in the  $y$  direction, the wave number can be estimated to be on the order of  $k\Omega_{ci}/v_{sh} \sim kr_g \sim 1$ , where  $r_g$  is the gyroradius of the downstream population. This is a great example of how dHybridR simulations can be directly compared with *in-situ* measured heliospheric plasma phenomena.

## 6. CONCLUSION

In this work we presented the first results from dHybridR, a hybrid plasma simulation code that includes relativistic ion dynamics. We detail how relativistic ion motion is included in the code and how for specific systems of interest, the assumptions required for hybrid simulations are not violated. This novel simulation software can be used to help understand, from

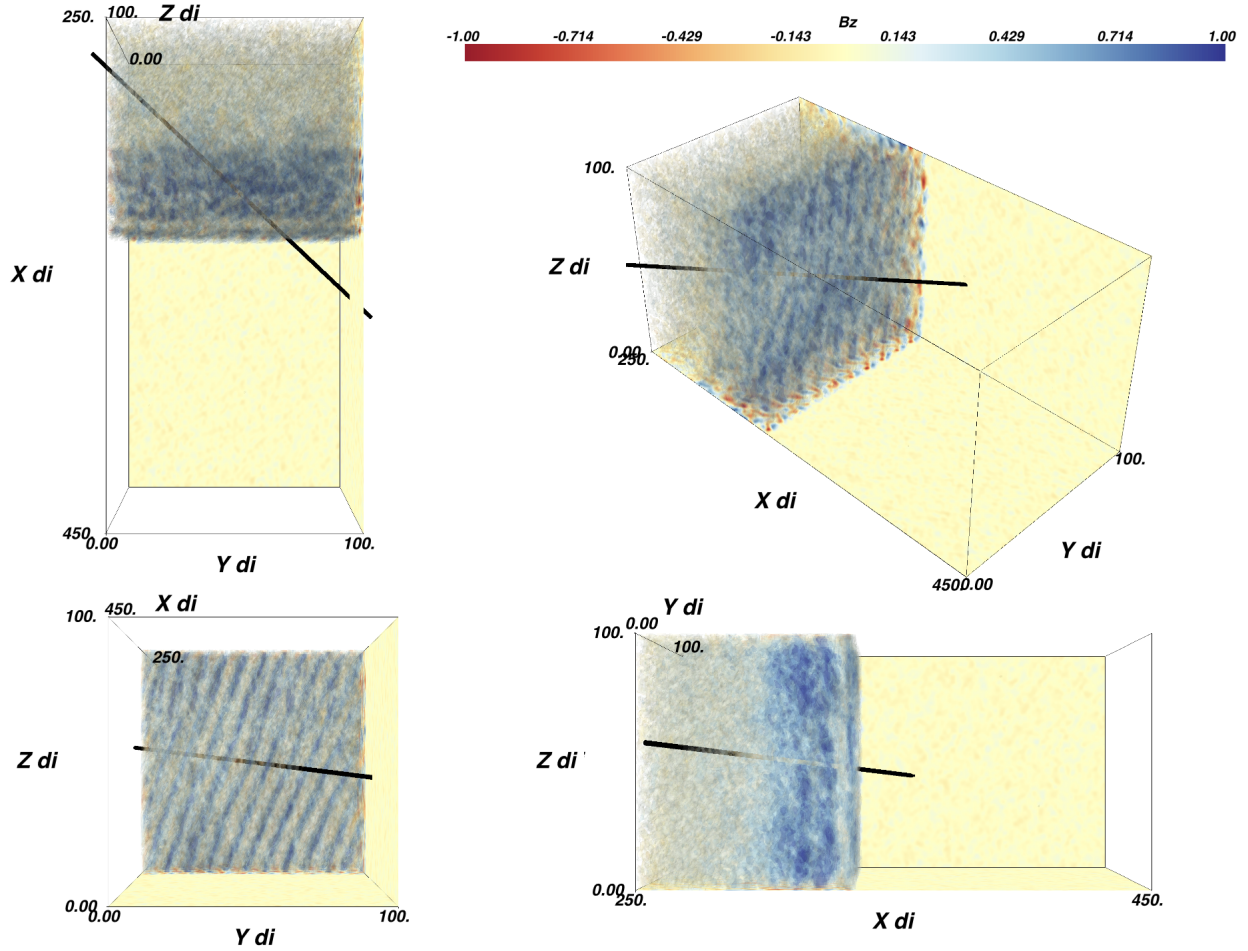


**Figure 11.** Orthographic projection of  $B_z$  (self-generated component normal to the upstream flow and mean magnetic field) around the shock from Run 3D. Four views of the 3D structure, with the following views from bottom right in clockwise order: viewing along  $+\hat{y}$ , along  $-\hat{x}$ , along  $-\hat{z}$  and an isometric view along  $(-\hat{x} + \hat{y} - \hat{z})/\sqrt{3}$ . Slices of  $B_z$  in the  $x$ ,  $y$  and  $x, z$  are plotted along the edge of the plotting domain. The black line represents the trajectory of the 1D cut shown in Figure 12.

first principles, numerous different open problems involving space and astrophysical plasmas. The code is well suited to study many astrophysical systems where a high energy, low density CR population interacts with a non-relativistic thermal background population.

To verify that **dHybridR** can correctly model physical systems of interest, we simulated CR-driven non-resonant and resonant streaming instabilities. In both test cases, the location in  $k$  space and the value of the maximum growth rate found in simulations agreed remarkably well with the linear prediction. Then, we moved to use **dHybridR** to model strongly non-linear problems such as DSA at non-relativistic collisionless shocks, similar to those found in the heliosphere, in SN remnants, and in galaxy clusters. In particular, we presented simulations with parameters relevant to fast

SN shocks (radio SNe, Figure 3) as well as heliospheric shocks such as the Earth’s bow shock (Figure 11).

We performed unprecedentedly-long simulations of parallel shocks in which ions achieve Lorentz factors as large as  $\gamma \gtrsim 20$ , attesting for the first time in full hybrid simulations that DSA produces a power-law tail in momentum across the trans-relativistic regime, which implies an energy distribution that follows a broken power law that steepens by 0.5 in slope. When CRs become relativistic, the increase of the maximum particle energy is still linear in time, but with a rate reduced by a factor of  $\sim 2$ ; such a reduction is a consequence of the saturation of the velocity of escaping particles to  $c$ .

The acceleration efficiency (i.e., the fraction of the shock energy channelled into non-thermal particles with energy  $E \gtrsim 10E_{sh}$ ) was found to reach about 10% within tens of cyclotron times and remain nearly constant as

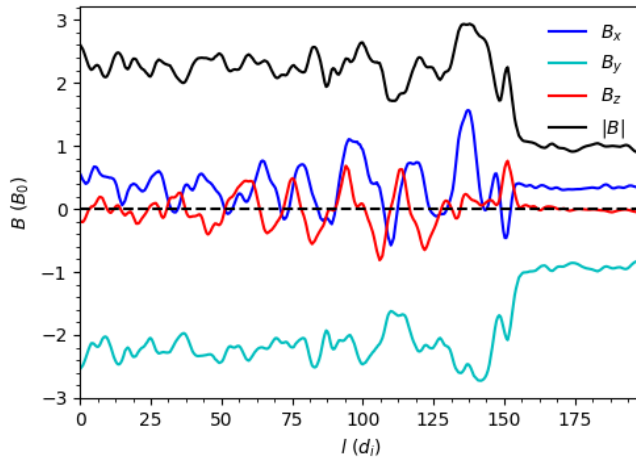


**Figure 12.** The 3 components and magnitude of the magnetic field along an oblique trajectory across the shock (from Run 3D Table 1). The trajectory is denoted by the black line in 3D projection view in Figure 11.

the high energy population transitions into the relativistic regime. These results are directly applicable to fast radio SNe, where we predict GeV/TeV CRs to be produced within seconds/days. With the current sensitivity

of  $\gamma$ -ray and neutrino telescopes, such a delay could be measured for a Galactic SN.

Finally, we presented a 3D simulation produced with dHybridR with conditions comparable to the Earth’s bow shock with a quasi-perpendicular configuration. We showed that dHybridR reproduces both qualitatively and quantitatively the shock rippling that has been found with *in-situ* satellite observations (Johlander et al. 2018).

In summary, this work presents, to the authors’ knowledge, the first hybrid simulations to include relativistic ion dynamics, which is a critical tool for studying the inherently multi-scale nature of CR/thermal ion interplay in space and astrophysical plasmas.

We would like to thank Luis Gargate for providing the original version of dHybrid. This research was partially supported by NASA (grant NNX17AG30G, 80NSSC18K1218, and 80NSSC18K1726) and NSF (grants AST-1714658 and AST-1909778). Simulations were performed on computational resources provided by the University of Chicago Research Computing Center, the NASA High-End Computing Program through the NASA Advanced Supercomputing Division at Ames Research Center, and XSEDE TACC (TG-AST180008).

## REFERENCES

- Amato, E., & Blasi, P. 2009, MNRAS, 392, 1591
- Bai, X.-N., Caprioli, D., Sironi, L., & Spitkovsky, A. 2015, ApJ, 809, 55
- Bell, A. R. 1978, MNRAS, 182, 147.  
[http://adsabs.harvard.edu/cgi-bin/nph-bib\\_query?bibcode=1978MNRAS.182..147B&db\\_key=AST](http://adsabs.harvard.edu/cgi-bin/nph-bib_query?bibcode=1978MNRAS.182..147B&db_key=AST)
- . 2004, MNRAS, 353, 550.  
[http://adsabs.harvard.edu/cgi-bin/nph-bib\\_query?bibcode=2004MNRAS.353..550B&db\\_key=AST](http://adsabs.harvard.edu/cgi-bin/nph-bib_query?bibcode=2004MNRAS.353..550B&db_key=AST)
- Bell, A. R., Robinson, A. P. L., Sherlock, M., Kingham, R. J., & Rozmus, W. 2006, Plasma Physics and Controlled Fusion, 48, R37. <https://doi.org/10.1088%2F0741-3335%2F48%2F3%2Fr01>
- Birdsall, C. K., & Langdon, A. B. 1991, Plasma Physics via Computer Simulation (CRC Press).  
<http://adsabs.harvard.edu/abs/1991ppcs.book.....B>
- Blasi, P., Amato, E., & Caprioli, D. 2007, Monthly Notices of the Royal Astronomical Society, 375, 1471.  
<http://dx.doi.org/10.1111/j.1365-2966.2006.11412.x>
- Burgess, D., Hellinger, P., Gingell, I., & Travnıcek, P. M. 2016, Journal of Plasma Physics, 82, 905820401
- Burgess, D., Mobius, E., & Scholer, M. 2012, SSRv, 173, 5
- Byers, J. A., Cohen, B. I., Condit, W. C., & Hanson, J. D. 1978, Journal of Computational Physics, 27, 363
- Caprioli, D., Pop, A., & Spitkovsky, A. 2015, ApJ Letters, 798, 28
- Caprioli, D., & Spitkovsky, A. 2014a, ApJ, 783, 91
- . 2014b, ApJ, 794, 46
- . 2014c, ApJ, 794, 47
- Caprioli, D., Zhang, H., & Spitkovsky, A. 2018, JPP, arXiv:1801.01510.  
<http://adsabs.harvard.edu/abs/2018arXiv180101510C>
- Chevalier, R. A., & Fransson, C. 2006, ApJ, 651, 381.  
<http://adsabs.harvard.edu/abs/2006ApJ...651..381C>
- Crumley, P., Caprioli, D., Markoff, S., & Spitkovsky, A. 2019, MNRAS, 485, 5105.  
<http://adsabs.harvard.edu/abs/2019MNRAS.485.5105C>
- Dubois, Y., Commercon, B., Marcowith, A. r., & Brahimı, L. 2019, arXiv e-prints, arXiv:1907.04300
- Gargate, L., Bingham, R., Fonseca, R. A., & Silva, L. O. 2007, Comp. Phys. Commun., 176, 419
- Gargate, L., Fonseca, R. A., Niemiec, J., et al. 2010, ApJL, 711, L127
- Gargate, L., & Spitkovsky, A. 2012, ApJ, 744, 67

- Giacalone, J. 2005, *ApJL*, 628, L37.  
<http://adsabs.harvard.edu/abs/2005ApJ...628L..37G>
- Giacalone, J., Burgess, D., Schwartz, S. J., & Ellison, D. C. 1992, *Geophys. Res. Lett.*, 19, 433
- Giacalone, J., Burgess, D., Schwartz, S. J., Ellison, D. C., & Bennett, L. 1997, *J. Geophys. Res.*, 102, 19789
- Hewett, D. W., & Nielson, C. W. 1978, *Journal of Computational Physics*, 29, 219
- Johlander, A., Vaivads, A., Khotyaintsev, Y. V., et al. 2018, *Plasma Physics and Controlled Fusion*, 60, 125006.  
<https://doi.org/10.1088%2F1361-6587%2Faae920>
- Johlander, A., Schwartz, S. J., Vaivads, A., et al. 2016, *Physical Review Letters*, 117, 165101.  
<http://adsabs.harvard.edu/abs/2016PhRvL.117p5101J>
- Jokipii, J. R. 1987, *ApJ*, 313, 842.  
<http://adsabs.harvard.edu/abs/1987ApJ...313..842J>
- Karimabadi, H., Roytershteyn, V., Vu, H. X., et al. 2014, *Physics of Plasmas*, 21, 062308
- Kulsrud, R., & Pearce, W. P. 1969, *ApJ*, 156, 445
- Kunz, M. W., Stone, J. M., & Bai, X.-N. 2014, *Journal of Computational Physics*, 259, 154.  
<http://adsabs.harvard.edu/abs/2014JCoPh.259..154K>
- Lagage, P. O., & Cesarsky, C. J. 1983a, *A&A*, 118, 223.  
<http://adsabs.harvard.edu/abs/1983A26A...118..223L>
- Lapenta, G. 2012, *Journal of Computational Physics*, 231, 795
- Le, A., Egedal, J., Daughton, W., Fox, W., & Katz, N. 2009, *Physical Review Letters*, 102, 085001.  
<http://adsabs.harvard.edu/abs/2009PhRvL.102h5001L>
- Lipatov, A. S. 2002, *The hybrid multiscale simulation technology: an introduction with application to astrophysical and laboratory plasmas* (Berlin; New York: Springer, Scientific computation)
- Lowe, R. E., & Burgess, D. 2003, *Annales Geophysicae*, 21, 671. <https://www.ann-geophys.net/21/671/2003/>
- Lucek, S. G., & Bell, A. R. 2000, *MNRAS*, 314, 65.  
[http://adsabs.harvard.edu/cgi-bin/nph-bib\\_query?bibcode=2000MNRAS.314..65L&db\\_key=AST](http://adsabs.harvard.edu/cgi-bin/nph-bib_query?bibcode=2000MNRAS.314..65L&db_key=AST)
- Mignone, A., Bodo, G., Vaidya, B., & Mattia, G. 2018, *The Astrophysical Journal*, 859,  
doi:10.3847/1538-4357/aabccd
- O’C. Drury, L. 1983, *Reports of Progress in Physics*, 46, 973.  
<http://adsabs.harvard.edu/abs/1983RPPh...46..973D>
- Palmroth, M., Ganse, U., Pfau-Kempf, Y., et al. 2018, *Living Reviews in Computational Astrophysics*, 4, 1
- Park, J., Caprioli, D., & Spitkovsky, A. 2015, *Physical Review Letters*, 114, 085003
- Skilling, J. 1975a, *MNRAS*, 172, 557.  
<http://adsabs.harvard.edu/abs/1975MNRAS.172..557S>
- Valentini, F., Trvnek, P., Califano, F., Hellinger, P., & Mangeney, A. 2007, *Journal of Computational Physics*, 225, 753. <http://www.sciencedirect.com/science/article/pii/S0021999107000022>
- van Marle, A. J., Casse, F., & Marcowith, A. 2018, *MNRAS*, 473, 3394.  
<http://adsabs.harvard.edu/abs/2018MNRAS.473.3394V>
- Weidl, M. S., Winske, D., & Niemann, C. 2019, *The Astrophysical Journal*, 872, 48.  
<https://doi.org/10.3847%2F1538-4357%2Faaafad0>
- Winske, D., & Omid, N. 1996, *J. Geophys. Res.*, 101, 17287
- Zachary, A. L., & Cohen, B. I. 1986, *Journal of Computational Physics*, 66, 469
- Zweibel, E. G. 2003, *ApJ*, 587, 625.  
<http://adsabs.harvard.edu/abs/2003ApJ...587..625Z>